Simulating Magnetohydrodynamically- Controlled Aerocapture and Comparing to its Atmospherically Controlled Counterpart

AE 8900 MS Special Problems Report
Space Systems Design Laboratory (SSDL)
Guggenheim School of Aerospace Engineering
Georgia Institute of Technology
Atlanta, GA

Author:
Danny N. Nguyen

Advisor:
Prof. Brian C. Gunter

December 15, 2021

Simulating Magnetohydrodynamically-Controlled Aerocapture and Comparing to its Atmospherically Controlled Counterpart

Danny N. Nguyen[1]
Georgia Institute of Technology, Atlanta, GA, 30313, USA

Soumyo Dutta[2] and Robert W. Moses[3]
NASA Langley Research Center, Hampton, VA, 23666, USA

Brian C. Gunter[4]
Georgia Institute of Technology, Atlanta, GA, 30313, USA

Throughout the past few decades, the demand for farther and more massive missions have increased significantly, especially with the recent push for manned missions to Mars as well as the growing scientific interest in the outer gas giants and their respective moons. While spacecraft have successfully made it to the surface of Mars or through the holds of outer planets, the technologies from these missions are reaching the threshold of their abilities. Thus, one of the most commonly proposed solutions is atmospheric aerocapture. By using a planet's atmosphere to slow down and guide the spacecraft into some target orbit, the spacecraft can save mass by significantly reducing the required corrective propellant burns. By saving the mass initially required for corrective maneuvers, the spacecraft can then reallocate this mass to increase the payload or increase the available propellant. However, while atmospheric aerocapture has its advantages over solely propellant-based missions, it may not be the best alternative because of its required increase in TPS mass to survive the deeper atmospheric pass. Although these mass savings outweigh the additional TPS mass, an alternative which can reduce both would be ideal. Magnetohydrodynamically-controlled aerocapture has the potential to serve as this alternative. Through NASA Langley's high-fidelity Program to Optimize Simulated Trajectories II, both atmospheric and magnetohydrodynamic aerocapture methods were simulated and compared for identical missions to Neptune. While their aerodynamic, aeroheating, and atmospheric models were provided by POST2, the required electrical conductivity and magnetohydrodynamic force models were created for this research. After a guidance algorithm was applied for both control methods, the results proved that, in nominal conditions, magnetohydrodynamics has not only the control authority to successfully capture but also the unique advantage of decreasing the sensed acceleration, maximum heat load, and TPS mass while doing so.

I. Nomenclature

α	=	angle of attack
β	=	side-slip angle
σ	=	bank angle

[1] Master's Student, Daniel Guggenheim School of Aerospace Engineering.
[2] Aerospace Engineer, Atmospheric Flight and Entry Systems Branch.
[3] Aerospace Technologist, Atmospheric Flight and Entry Systems Branch.
[4] Associate Professor, Daniel Guggenheim School Aerospace Engineering, Senior Member AIAA.

$\vec{D}$	=	drag force vector
$\vec{L}$	=	lift force vector
$\vec{Q}$	=	side force vector
$\hat{x}_b$	=	body frame x-axis
$\hat{y}_b$	=	body frame y-axis
$\hat{z}_b$	=	body frame z-axis
$\vec{V}_\infty$	=	freestream velocity vector
B_x	=	x-component of the magnetic field vector
B_y	=	y-component of the magnetic field vector
B_z	=	z-component of the magnetic field vector
B_0	=	magnetic field vector
Φ	=	magnetohydrodynamic pitch angle
u_1	=	pre-shock atmospheric velocity
u_2	=	post-shock local velocity
I	=	electromagnetic current
σ_e	=	electrical conductivity
μ_0	=	permeability of vacuum
r_c	=	electromagnet coil radius
N	=	number of turns in the electromagnet
m	=	electromagnet mass
A_w	=	wire cross-sectional area
l_w	=	wire length
ρ_w	=	wire mass density
P	=	electromagnet power
σ_w	=	wire electrical conductivity
t_{fuse}	=	electrical fusing time
T_{melt}	=	material melting temperature in Celsius
T_{init}	=	material initial temperature in Celsius
n_e	=	electron number density
n	=	gas number density
T_e	=	electron temperature
F_x	=	x-component of the Lorentz force vector
F_y	=	y-component of the Lorentz force vector
F_z	=	z-component of the Lorentz force vector
K	=	load factor
A_{patch}	=	MHD patch area

II. Introduction

Throughout the past few decades, the desire for space exploration has grown significantly; however, the technology used to do so has remained relatively the same. While chemical propulsion, parachutes, and inflatables make current missions to the Moon and Mars feasible, these technologies are limited for future manned missions to Mars and beyond. These traditional methods are inadequate for larger and farther missions due to the inherent mass constraints of solely using propellant. Thus, there has been an ongoing effort to introduce new methods of deceleration and flight control during planetary entry, descent, and landing to reduce the required propellant mass and enable new missions. One of the most prominently proposed solutions is atmospheric aerocapture.

Aerocapture is the use of a planet's atmosphere to modulate the lift and drag forces acting on the spacecraft and "capture" into an orbit around that planet. As shown in Fig. 1 from Ref. [1], the spacecraft will enter hyperbolically into the atmosphere, begin its guidance to be put onto a trajectory towards some target parking orbit, and then finally perform a few corrective maneuvers to adjust for any inevitable uncertainties or perturbations. While these corrective maneuvers will require propulsive burns, these burns will be considerably less than the burns that would have been required if aerocapture had not been applied. It is the goal of the controlled guidance to minimize the required propulsive burns for these corrective maneuvers while consistently capturing in the desired orbit. By taking advantage of the induced forces on a spacecraft, propellant burns can be compensated, allowing for a significant reduction in the required propellant mass. By reducing the propellant mass needed for maneuvers, this mass can be reallocated to make

the spacecraft larger and accommodate manned missions, or the saved mass could also be repurposed to allow for missions farther into the solar system.

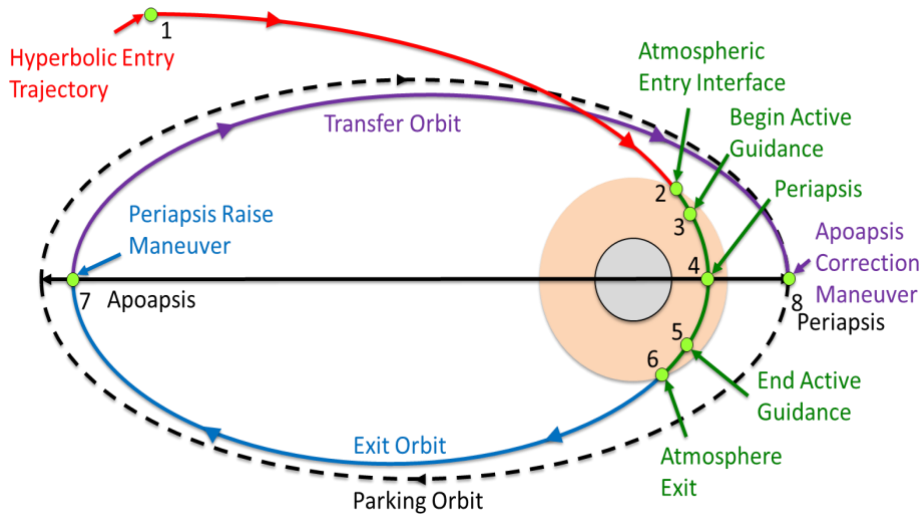

Fig. 1 Aerocapture concept of operations.

In atmospheric aerocapture, specifically, the controlled guidance is performed in one of three ways: direct force control (DFC), bank angle modulation (BAM), or drag control. However, the primary methods considered in this report are only DFC and BAM since they are controlled solely with the vehicle's aerodynamic angles. Direct force control actively adjusts the angle of attack and the side slip angle to directly manipulate the lift and drag vectors and force the spacecraft in different directions. On the other hand, bank angle modulation actively adjusts the bank angle to essentially roll the spacecraft and indirectly change the direction of the forces on the vehicle. The effects these aerodynamic controls have on the resulting forces on the vehicle are visualized in Fig. 2 from Ref. [1] below.

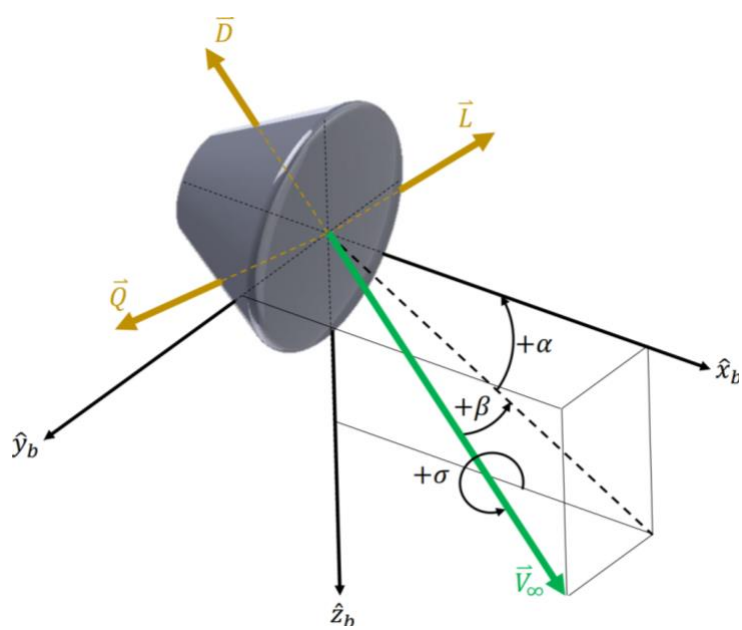

Fig. 2 Aerodynamic angles and their effects on various aerodynamic forces

While the benefits of atmospheric aerocapture have been studied for several years now, it is still unclear if this method is the best alternative to traditional propulsive maneuvers. While research studies have proven considerable

reductions in propellant mass with the use of atmospheric aerocapture, relying on the atmospheric density and the resulting aerodynamic forces poses a few disadvantages. First, for planets with a less dense atmosphere, the control authority atmospheric aerocapture allows is limited. More importantly, having the control authority directly related to the density of the atmosphere restricts the spacecraft to have to pass deep into a planet's atmosphere to achieve enough force to guide the spacecraft. Because of this, the thermal protection system on the spacecraft must be more robust in order to survive the pass. Thus, although saving propellant mass, atmospheric aerocapture must add considerable thermal protection system mass in return. Although these propellant savings still outweigh this additional TPS mass, an alternative which reduces both the propellant mass and the TPS mass would be the ideal solution to begin enabling these previously infeasible missions.

This research proposes magnetohydrodynamics as that solution. Magnetohydrodynamics (MHD) essentially takes advantage of the electrically conductive, ionized plasma that is created during the spacecraft's hypersonic entry into a planet's atmosphere. By introducing a controllable magnetic field through an onboard electromagnet to this surrounding conductive plasma, Lorentz forces can be created. These Lorentz forces can then be directed by manipulating the electromagnet(s) and their subsequent magnetic field components. These induced Lorentz forces can then supplement or even replace aerodynamic forces as a control method in aerocapture. In fact, solely MHD-controlled aerocapture is theorized to have the potential to have a unique advantage over its traditional atmospherically controlled counterpart because of its ability to be activated much higher in the atmosphere while still achieving the same magnitudes of force and control authority. Thus, MHD-controlled aerocapture has the potential to not only achieve propellant mass reductions on par with that of its atmospheric counterpart but also minimize TPS mass.

III. Problem Formulation

This research project serves to prove MHD-controlled aerocapture can improve upon its atmospheric predecessor. Before simulating and comparing the two approaches, it is important to define how each will physically function on the spacecraft. First, the aerodynamic angle modulations required for both DFC and BAM can be controlled through either an internal ballast which applies a torque about the spacecraft's center of gravity or an external aerodynamic control surface, such as a flap, to tilt and rotate the spacecraft. On the other hand, the mechanisms to modulate magnetohydrodynamic control are a bit more complex. Magnetohydrodynamics is typically applied using an electromagnet; however, in this case, a configuration of two electromagnets is used instead. Since the goal of MHD in this research is to manipulate the forces on the spacecraft, the Lorentz forces created must have the ability to be magnified and directed as the guidance sees fit. The magnitude of the Lorentz force can be directly controlled by changing the current going through the electromagnet since that is directly proportional to the magnetic field strength and thus, the induced force.

The direction of the Lorentz force vector, on the other hand, can be changed in two different ways. The first method is to simply rotate a single electromagnet inside the spacecraft to direct the force as necessary. Although it may seem simpler in theory, this method would require a complex system to maneuver the electromagnet, and the moving parts leave room for more potential problems. The second method and the one used in this research is to configure two static electromagnets, one in the body frame x-axis and one in the body frame z-axis, as shown in Fig. 2 below. Current will be applied to each electromagnet separately to change the magnitude of each component of the magnetic field. By manipulating the current to each electromagnet, the MHD pitch angle can be controlled, and the resulting magnetic field vector and force vector can be directed as necessary. An important note to make about this configuration is that both electromagnets are configured at the spacecraft's center of gravity. This ensures ballistic entry and prevents the spacecraft from rotating and producing any incidental aerodynamic angles and forces. This is preferred for the purposes of this research because it ensures that the control and subsequent aerocapture are solely due to magnetohydrodynamic control and not due to any additional aerodynamic forces if the spacecraft rotates. In reality, this configuration would likely be closer to the ionized plasma at the surface of the spacecraft to allow for higher control authority; however, since this research serves as only a proof of concept of MHD-controlled aerocapture, isolating the MHD control is ideal.

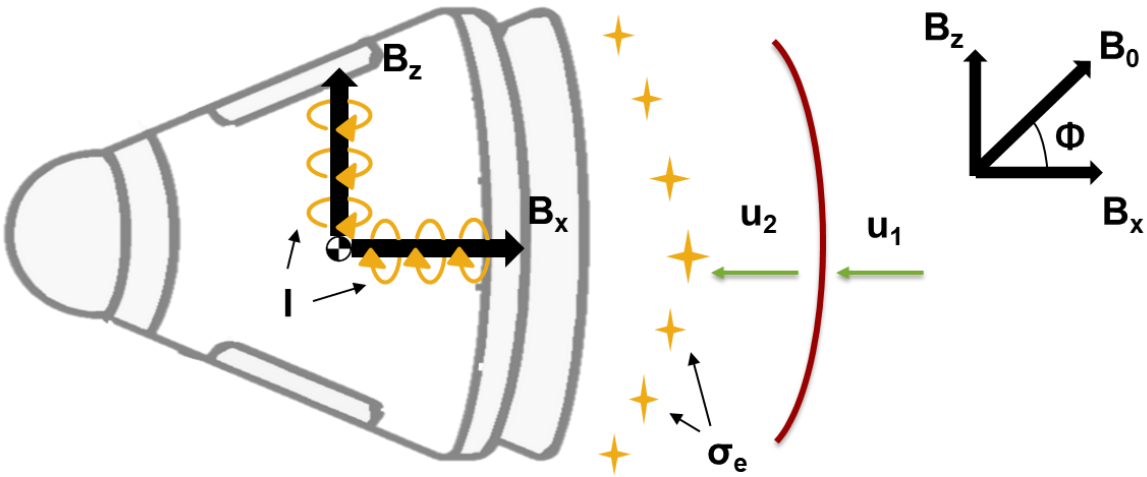

Fig. 3 Electromagnet configuration for MHD-controlled aerocapture

With the electromagnet configuration decided, only the electromagnets themselves were left to be designed. The preliminary design for each electromagnet focused on achieving a functional magnetic field strength while minimizing the electromagnet's mass and required power. Another important design factor was the fusing time of each electromagnet's wires; the wires had to survive long enough to guide the spacecraft towards the target orbit without melting from the strength of the current. The magnetic field strength is related to the physical design of the electromagnet based on the Biot-Savart Law given in Eq. (1) below. The only factor which actively and proportionally changes the magnetic field strength in this equation is the electrical current in the electromagnet. The mass and power constraints to the design are both heavily dependent on the characteristics of the selected wire. These constraints are fully defined by Eqs. (2), (3), and (4) below. Finally, the electrical fusing time is defined through Onderdonk's equation shown in Eq. (5) where the initial wire temperature is set to be twenty degrees Celsius or roughly room temperature. This serves as a conservative preliminary estimate of the fusing time because the initial temperature will likely be lower than room temperature in actual applications, and thus, the actual fusing times will likely be higher.

$$B_0 = \frac{N\mu_0}{2r_c} * I \tag{1}$$

$$m = A_w l_w \rho_w \tag{2}$$

$$l_w = 2\pi r_c N \tag{3}$$

$$P = \frac{4\pi r_c^2}{\mu_0 A_w \sigma_w} * B_0 I \tag{4}$$

$$t_{fuse} = 1.15 * 10^5 \log_{10}\left(\frac{T_{melt} - T_{init}}{233 + T_{init}} + 1\right)\left(\frac{A_w}{I}\right)^2 \tag{5}$$

The mass and power are not only dependent on the physical size and length of the wire but also the wire's mass density and electrical conductivity. The most common materials used for electromagnetic coil wires are copper and aluminum. While copper is more electrically conductive, it is also more physically dense; thus, the material choice

becomes a tradeoff between power and mass. On top of that, the melting point of copper is higher than that of aluminum which inherently allows the fusing time of copper wires to be higher than that of aluminum. Varying only the wire material, the trade study between the two is shown in Table 1. While aluminum requires more power and lasts a shorter amount of time than copper, its mass difference significantly outweighs the disadvantages in power and fusing time. Thus, aluminum was chosen as the electromagnet material type moving forward.

Table 1 Wire material trade study

	Copper	Aluminum	Percent Difference, %
Mass, kg	119.8	36.23	107.11
Power, W	6,285	9,913	44.80
Electrical Fusing Time, s	2,946	2252	26.71

Finally, after choosing the wire material, the electromagnet design becomes a multivariable optimization problem, minimizing mass and power while maximizing the magnetic field strength and fusing time. The variables which directly affect this optimization are the electromagnetic current, coil radius, cross-sectional wire area, and number of turns. These four variables were altered until a reasonable mass, power, magnetic field strength, and fusing time were all achieved. For the purposes of this research, the preliminary point design for a single electromagnet defined in Table 2 will suffice; however, future research efforts may perform more robust optimization to achieve an optimal electromagnet design.

Table 2 Electromagnet point design

Design Parameter	Value
Max Current, A	70.35
Coil Radius, m	0.10
Wire Gauge, AWG	6
Number of Turns	1,600
Mass, kg	36.23
Max Required Power, W	9,913
Max Magnetic Field Strength, T	0.707
Min Fusing Time, s	2,252

Table 2 refers to several of the design parameters as the maximum or minimum value for that variable. This is because the current to each electromagnet can be adjusted between zero and the listed maximum value, and since mass, power, and fusing time are functions of this current, these variables will all change with the current. It is important to note that Table 2 is only referring to the design parameters for a single electromagnet and not the electromagnet configuration. Thus, Table 3 depicts the variables of interest for the entire electromagnet configuration.

Table 3 Design considerations for the two-electromagnet configuration

Design Parameter	Value
Mass, kg	72.46
Max Required Power, W	19,826
Min Fusing Time, s	2,252

Although these tables have defined these design considerations as necessary, these values have no reference to indicate if these numbers are reasonable or even feasible. First, based on previous research using atmospheric aerocapture for trajectories to Neptune, the required thermal protection system mass to support the atmospheric pass was roughly 556.6 kilograms [2]. This means the additional mass from the electromagnetic configuration is roughly 13% of the TPS mass typically required for atmospherically controlled aerocapture. Thus, if the TPS mass savings are significantly greater than 13% of its original mass, then MHD-controlled aerocapture may prove to be the ideal enabler

for larger and farther missions. Next, although the power required may seem daunting, this power can be created through magnetohydrodynamic power generation. Previous research have proven MHD power generation to create usable power on the order of hundreds of kilowatts [3, 4]. Thus, the electromagnetic configuration can actually power itself and more. Finally, the fusing time of the electrical wire in the configuration is roughly 2,300 seconds. Previously performed atmospheric aerocapture studies have found the guidance to last typically under 1,000 seconds [1]. Thus, if magnetohydrodynamics can perform on par with its atmospheric counterparts, this fusing time should be more than enough.

IV. Simulating MHD-Controlled Aerocapture

A. Simulation Models shared by Atmospheric and Magnetohydrodynamic Aerocapture

To allow for a direct comparison between MHD-controlled aerocapture and atmospherically controlled aerocapture, the simulations were made as identical as possible with the main difference only being the control method. These trajectory simulations were both created in NASA Langley's high-fidelity Program to Optimize Simulated Trajectories II or POST2. This program allowed for precise trajectory integration and optimization while using robust spacecraft aerodynamic and aeroheating models as well as planetary gravitational and atmospheric models. The models used for this research effort were predefined options built into the program which have years of history and extensive uses throughout several NASA missions and research efforts. The models used are listed in Table 4 below.

Table 4 Vehicular and planetary models used

	Model
Aerodynamic Model	MSL Aerodatabase
Aeroheating Model	Sutton-Graves
Gravitational Model	Unnormalized Oblate Planet Model up to J2
Atmospheric Model	2004 Neptune GRAM

The aerodynamic model chosen is essentially a well-defined blunt-body entry vehicle developed by the Mars Science Laboratory (MSL), and although these aerocapture simulations may not be to Mars, the vehicle shape and characteristics translate well to the similar entry and descent purposes of this research [5]. Next, the stagnation point heating rate and the associated heating integral are calculated using the planet's specific Sutton-Graves constant. The planet chosen for the purposes of both atmospheric and magnetohydrodynamic aerocapture was Neptune. Neptune serves as an ideal target because of its large need for mission-enabling mass savings as well as its relatively dense atmosphere when compared to not only other gas giants but also other primary scientific bodies of interest such as Mars. Lastly, the gravitational model for Neptune was defined by an oblate planetary model using Neptune's J2 constant while the atmospheric mode for Neptune was defined by a 2004 Neptune Global Reference Atmosphere Model (GRAM). In short, the 2004 Neptune GRAM allows for an in-depth model of the mean and perturbed density, speed of sound, and wind profiles at different times and locations on Neptune.

While these shared models define all of the necessary factors playing a role in atmospheric aerocapture and several of the key components in MHD-controlled aerocapture, MHD-control cannot exist without two crucial additions: the electrical conductivity model and the MHD-induced Lorentz force model. The electrical conductivity model is critical because it determines the viability of the atmosphere during hypersonic entry and descent to create MHD control and forces. The MHD-induced Lorentz force model then calculates and applies these generated forces to the spacecraft. Without the latter, MHD-control would not be able to move and manipulate the spacecraft during the simulation.

B. Electrical Conductivity Model

The electrical conductivity of the spacecraft's surrounding atmosphere is directly proportional to the induced forces the spacecraft experiences; therefore, it is important to model the electrical conductivity correctly. The equations for the electrical conductivity are dependent on three different variables: the electron number density, the gas number density, and the electron temperature. A fourth variable, the ionization factor, is also relevant; however, it is derived as the fraction of the electron number density over the total gas number density. The ionization factor plays a role in the electrical conductivity model because the conductivity is defined at two different conditions: a low ionization factor and a high ionization factor. Equation (6) conveys this relationship.

$$\sigma = \begin{cases} 3 * 10^5 \left(\frac{n_e}{n}\right), & \frac{ne}{n} \leq 10^{-3} \\ 2.147 * 10^{-3} (T_e)^{\frac{3}{2}}, & \frac{ne}{n} > 10^{-3} \end{cases} \tag{6}$$

Thus, the electrical conductivity's accuracy is tied to the fidelity at which the electron number density, gas number density, and electron temperatures are known. Through the NASA Langley Aerothermodynamic Upwind Relaxation Algorithm (LAURA), a computational fluid dynamics simulation software code, these variables were calculated with confidence for a range of atmospheric density and velocity values. These variables were then defined in a multivariable lookup table that can be imported into and used by POST2 accordingly. The main caveat with this lookup table is that it is bounded by the atmospheric density from 10^{-6} to 10^{-3} kg/m^3 and by the atmospheric velocity from 16 to 32 km/s. While these bounds are appropriate for the range of velocities the spacecraft is expected to travel at, the lower bound of the density is not comprehensive of the range of densities magnetohydrodynamics can operate at. However, expanding the range of densities below 10^{-6} kg/m^3 requires a more complex direct simulation Monte Carlo solver instead of the currently used Navier-Stokes solver because of the rarefied flow below that density. Future research efforts may improve upon this model; however, for the purposes of this research, these variables will be logarithmically extrapolated for the range of densities below 10^{-6} until 10^{-10} kg/m^3 where any further electron number density, gas number density, and electron temperature will be considered negligible.

C. Magnetohydrodynamically-Induced Lorentz Force Model

With the electrical conductivity model defined, the magnetohydrodynamically-induced Lorentz force can be calculated and combined into the POST2 trajectory integration. Because of the ideal atmospheric conditions of Neptune with regards to MHD, the Hall effect and ion slip effects can be deemed negligible, and thus, the induced Lorentz side force can be ignored. This leaves the induced forces on the body x- and z-axes; these forces are calculated through Eqs. (7) and (8) below.

$$F_x = -(1 - K)\sigma u_2 B_z^2 A_{patch} \tag{7}$$

$$F_z = (1 - K)\sigma u_2 B_z B_x A_{patch} \tag{8}$$

First, the load factor is a constant defined by the relationship between the load resistance and the plasma resistance. This is a value between zero and unity, and for the purposes of this research, it was defined as a constant of 0.5. Future research efforts can change this value to perform a concrete case study of its effects; however, based on the Lorentz force equations, it can be seen that a higher load factor will give less control authority since the induced forces will be smaller and vice versa. Thus, this research chose 0.5 to serve as the prime case and allow for a general proof of concept. Next, the electrical conductivity is given by the previously discussed electrical conductivity model. The post-shock local velocity, on the other hand, is given using shock equations and calculations built into the POST2 software. For the same reasons as the force equations, the magnetic field calculations will also only consider the x- and z-axes components. The magnetic field components are defined by Eqs. (9) and (10).

$$B_x = B_0 \cos(\phi) \tag{9}$$

$$B_z = B_0 \sin(\phi) \tag{10}$$

These equations relate each component's magnitude to the magnitude of the full magnetic field vector as well as the MHD pitch angle. To simplify the targeting and optimization problem, the magnetic field vector magnitude is kept at a constant value so that the MHD pitch angle is the only independent variable. This essentially forces the electromagnet configuration's total electric current to remain constant. Thus, decreasing the current to one electromagnet will increase the current to the other electromagnet to keep the total current and magnetic field vector magnitude constant. In reality, this would be impractical, and the total current would decrease to conserve power as needed. However, because of the excess power available through MHD power generation, this simplification is feasible for the purposes of this research. Finally, the MHD patch area is the area over which the induced force acts, which is defined in relation to the electromagnetic coil radius in Eq. (11).

$$A_{patch} = \pi r_c^2 \tag{11}$$

After applying all of these equations into POST2, these new MHD-induced Lorentz forces were then integrated into the total force calculation to allow the vehicle to move and react to the additional forces accordingly.

V. Guidance Algorithms Settings and Convergence Results

After modeling the underlying physics of atmospheric and magnetohydrodynamic control, the guidance algorithm behind each control method can be developed. Whether open loop or closed loop guidance was applied, the goal of each guidance algorithm remained the same: to capture into a target orbit of interest. For this research to Neptune, the target orbit is defined by the orbital parameters in Table 5. This orbit was chosen because of its Triton flyby capability, maximizing the potential scientific benefit of this mission.

Table 5 Orbital parameters for Triton flyby target orbit

Orbital Parameter	Value
Apoapsis Altitude, km	430,000
Periapsis Altitude, km	3,986
Longitude of the Ascending Node, deg	330.829
Inclination, deg	153.547

A. Guidance Algorithm for Atmospheric Aerocapture

Aerodynamic aerocapture uses a robust numerical predictor-corrector algorithm to perform closed-loop guidance and optimize the aerodynamic angle as necessary. The algorithm used is NASA Langley's Fully Numerical Predictor-corrector Aerocapture Guidance algorithm or FNPAG. FNPAG is a well established and supported algorithm which can actively optimize multiple variables at once while targeting some given variable. For the direct force control case, the angle of attack and the side slip angles were actively optimized to target the mean apoapsis altitude of 430,000 km. The angle of attack was allowed to vary within negative and positive twenty degrees whereas the side slip angle was limited between negative and positive five degrees. Finally, the bank angle in the direct force control case was kept constant at zero because it had little effect on the optimization results.

On the other hand, for the bank angle modulation case, the bank angle was actively optimized to target the mean apoapsis altitude of 430,000 km. Since the bank angle affects the induced forces indirectly, it was allowed a much larger range of values from 15 to 165 degrees. Similar to the bank angle in the DFC case, the side slip angle in this case was set to zero because it had negligible effects on optimization results. However, the same is not true for the angle of attack. After performing multiple case studies altering the angle of attack, a constant angle of attack of -20° was found to give the best results.

Table 6 shows this case study and the effects the angle of attack had on the capture success and subsequent required corrective propellant burns. With steeper angles of attack, the control authority and the success increased until the angle of attack reached a stalling point where the success began to trade off with the propellant savings. In this case, the success was valued more than the saved propellant mass; thus, the angle of attack was set at the highest success rate case. These percentages are from case studies of 8,000 Monte Carlo runs each where the initial conditions, aerodynamic variables, and atmospheric parameters were perturbed to observe off-nominal conditions.

Table 6 Angle of attack Monte Carlo case study

Angle of Attack, [°]	Top Percentile Propellant Burn Required, [km/s]	Cases successfully captured, [%]	Cases crashed, [%]	Cases exited hyperbolically, [%]
-10	3481.9697	61.5625	38.4245	0.0125
-16	3241.3049	98.1625	1.8375	0
-18	3151.3650	99.8375	0.15	0.0125
-20	2637.1955	99.875	0	0.125
-22	1959.2060	99.7625	0	0.2375
-24	1024.3709	97.6625	0	2.3375

Both cases captured into the target orbit within a similar amount of time; however, the bank angle control case required a steeper entry flight path angle. This is an important distinction because the entry flight path angle plays a large role in the depth of the atmospheric pass the spacecraft requires. A steeper entry flight angle indicates a deeper pass which requires a more robust and more massive TPS system. Thus, the entry flight path angle has a direct relationship with the additional mass this research aims to minimize. The aerodynamic angle settings and required entry flight path angles for direct force control and bank angle modulation are summarized in Table 7 below.

Table 7 Aerodynamic angle settings and required entry flight path angle for atmospheric control

	Angle of Attack, [°]	Side Slip Angle, [°]	Bank Angle, [°]	Entry Flight Path Angle, [°]
Direct Force Control	$-20 \leq \alpha \leq 20$	$-5 \leq \beta \leq 5$	0	-12.355
Bank Angle Modulation	-20	0	$15 \leq \sigma \leq 165$	-12.600

B. Guidance Algorithm for Magnetohydrodynamic Aerocapture

On the other hand, the MHD-controlled aerocapture simulation utilizes open-loop guidance instead of the more robust closed-loop active guidance applied in its atmospheric counterpart. While closed-loop active guidance with off nominal Monte Carlo case studies would be ideal, proving the capabilities and advantages of the general, nominal MHD-controlled aerocapture first is also a crucial step. Future research efforts may build off the findings of this research by improving this guidance algorithm and applying perturbations in Monte Carlo case studies.

As mentioned in the electromagnet configuration design, the electromagnets were placed at the center of gravity of the spacecraft to ensure ballistic entry even when the MHD-induced forces begin to act on the spacecraft. Ballistic entry isolates the magnetohydrodynamic control to truly determine its capability alone as compared to its atmospheric counterpart. Thus, for the same reason, the aerodynamic angles will all be set to zero. Finally, the MHD pitch angle needs to be optimized to determine how power will be distributed to each electromagnet. In this case, the MHD pitch angle was set to 90° to allow for maximum force in the drag direction. This allows the spacecraft to slow down faster and minimize the entry flight path angle needed to successfully capture. Future applications may apply active guidance to manipulate this MHD pitch angle from this constant as needed. However, from preliminary tests, the optimal MHD pitch angle is found to be heavily weighted towards maximizing the drag force; thus, this closed loop case still serves as a strong representation of how MHD-controlled aerocapture will perform.

With the MHD pitch angle set at 90°, this essentially means that all of the current will flow to the z-axis-oriented electromagnet which then directs all of the induced Lorentz force in the negative body x-axis. By maximizing the z-component of the magnetic field vector and the subsequent induced drag force, the required entry flight path angle to successfully capture was reduced to -10.937°. As seen in Fig. (4) below, the isolated MHD-controlled aerocapture simulation successfully captured into the Triton-flyby orbit in a similar amount of time as the atmospheric aerocapture simulations. However, MHD-control was able to do so while reducing the entry flight path angle significantly. The parameters which achieved these results for magnetohydrodynamic control are summarized in Table 8 below.

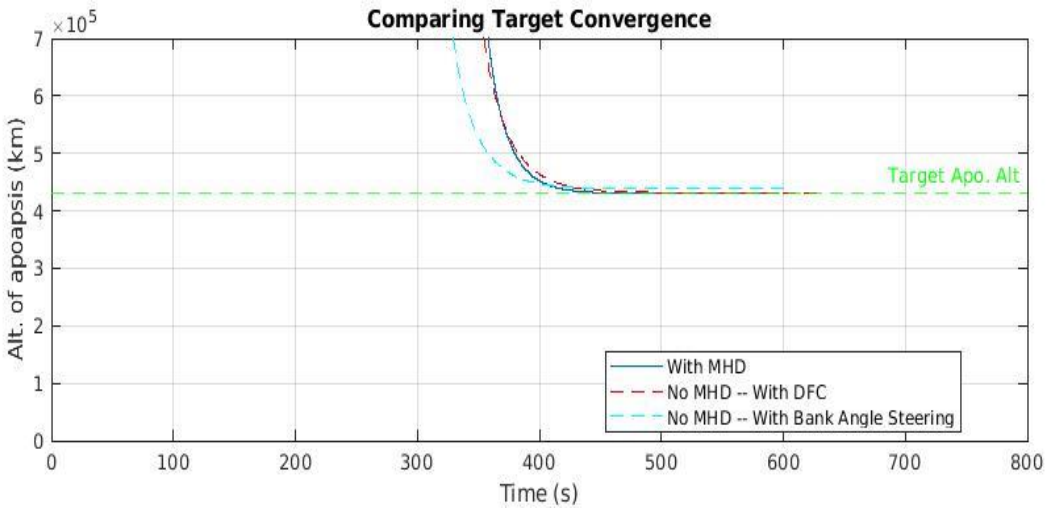

Fig. 4 Atmospheric and magnetohydrodynamic aerocapture target convergence results

Table 8 Aerodynamic and magnetohydrodynamic settings for MHD-control

Control Parameter	Value
Angle of Attack, [°]	0
Side Slip Angle, [°]	0
Bank Angle, [°]	0
MHD Pitch Angle, [°]	90
B_x, [T]	0
B_z, [T]	-0.704
Entry Flight Path Angle, [°]	-10.937

VI. Simulation Results and Comparisons

While the aerodynamic and magnetohydrodynamic settings for MHD-control have proven successful aerocapture, the performance of this control method over its atmospheric counterpart has yet to be truly quantified. Figure (5) b) shows the forces the MHD-control case experiences from the aerodynamic and MHD-induced forces throughout its pass. Because the MHD pitch angle was set to divert all of the power to the z-component of the magnetic field vector, only a drag force is induced. Similarly, because all of the aerodynamic angles were set to zero and the electromagnet configuration was placed at the center of gravity, the spacecraft flies ballistically, and the only aerodynamic force is in the drag direction as well. Both of these findings follow the expected behavior.

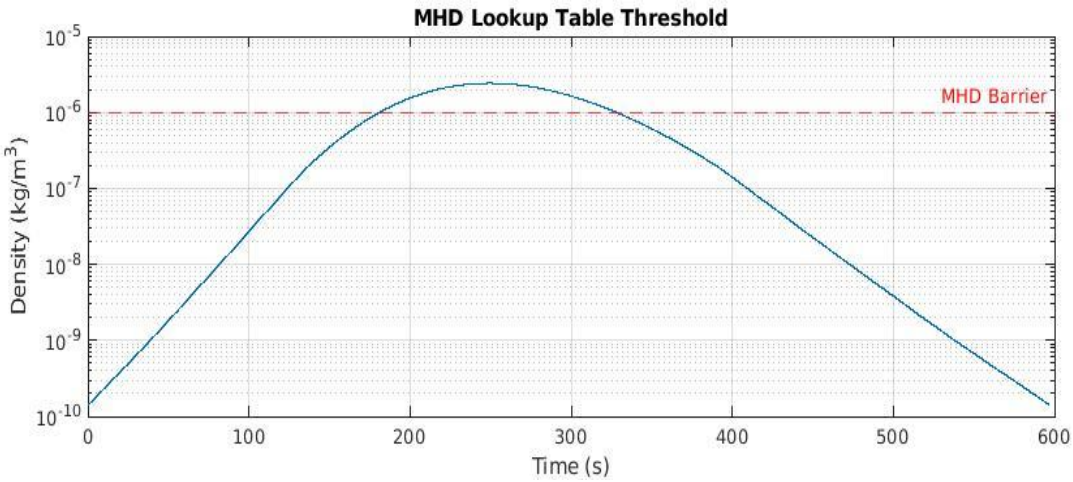

a)

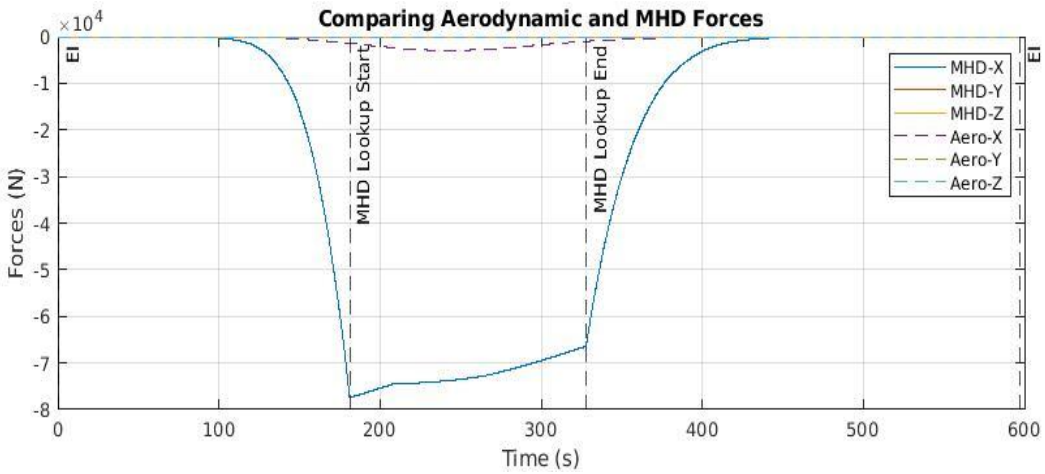

b)

Fig. 5 Aerodynamic and magnetohydrodynamic forces over a range of atmospheric densities

Figure (5) a) depicts the atmospheric density the spacecraft experiences as it passes through the planet's atmosphere. As mentioned before, the electrical conductivity for atmospheric densities below 10^{-6} kg/m^3 is logarithmically extrapolated until 10^{-10} kg/m^3. Since the electrical conductivity is directly proportional to the Lorentz forces, these logarithmic trends are seen in the force plot as well. When the atmospheric density is below the threshold for the high-fidelity MHD lookup table, the MHD force acts logarithmically; however, above this threshold, the MHD force does not behave in an expected manner. In fact, instead of completing a normal curve like atmospheric forces do, it almost linearly begins to decrease. While this may seem like odd behavior for atmospheric forces, this behavior follows the physics set by the magnetohydrodynamic equations.

When compared to the direct force control and bank angle modulation cases, the available drag force for the MHD-controlled case is roughly two-thirds or half of the available drag in each atmospheric case, respectively. These relations are illustrated in Fig. (6). While the available force is less than its atmospheric counterparts, this is not necessarily a disadvantage of magnetohydrodynamics. In fact, being able to still successfully capture with a smaller force is actually advantageous because it reduces the sensed acceleration the spacecraft has to endure. As seen in Fig. (7), the sensed acceleration is directly proportional to the total force the spacecraft experiences.

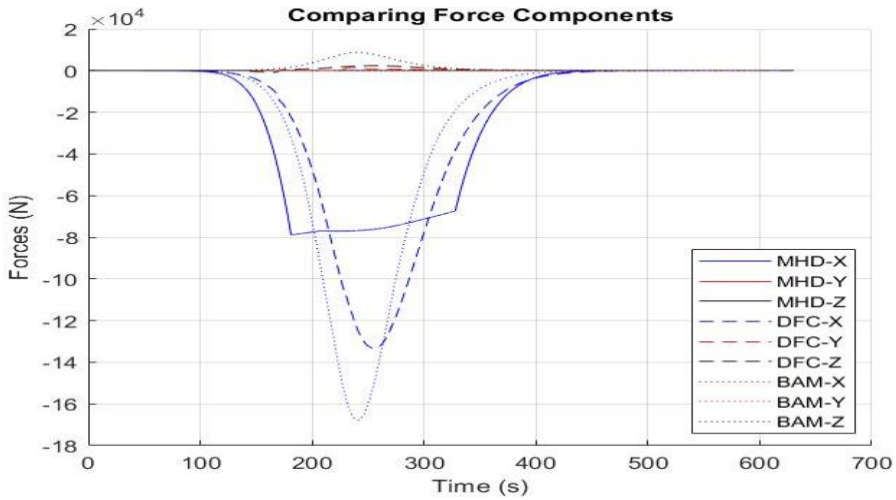

Fig. 6 Total force in each control method

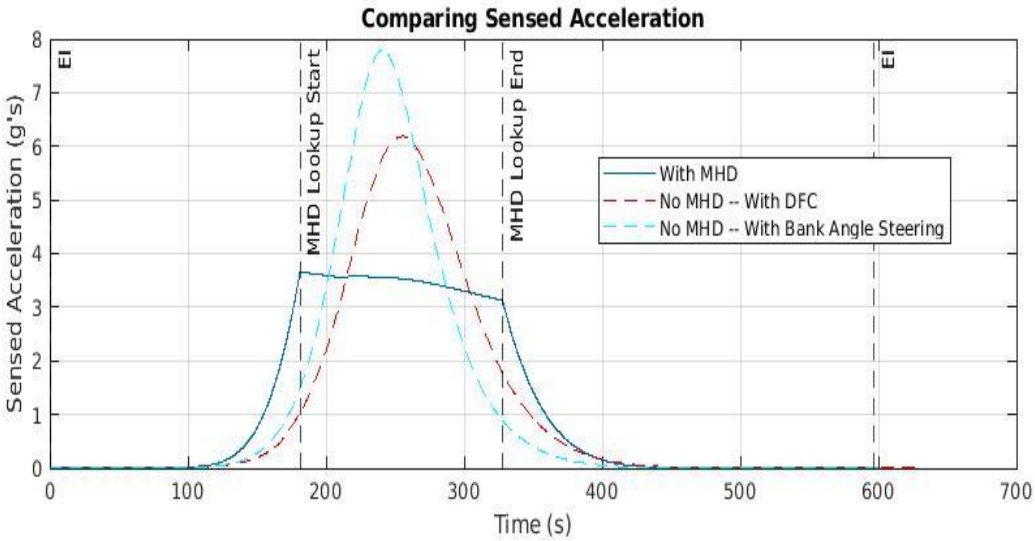

Fig. 7 Sensed acceleration in each control method

Finally, while the previously discussed guidance results proved that MHD-controlled aerocapture allows for successful capture with a much shallower entry flight path angle, we have yet to quantitatively prove the implications of this finding. The shallower flight path angle allows the spacecraft to pass through the atmosphere at a much higher altitude. This pass is shown in Fig. (8) where the MHD-controlled pass is almost 200 kilometers higher than the atmospherically controlled passes.

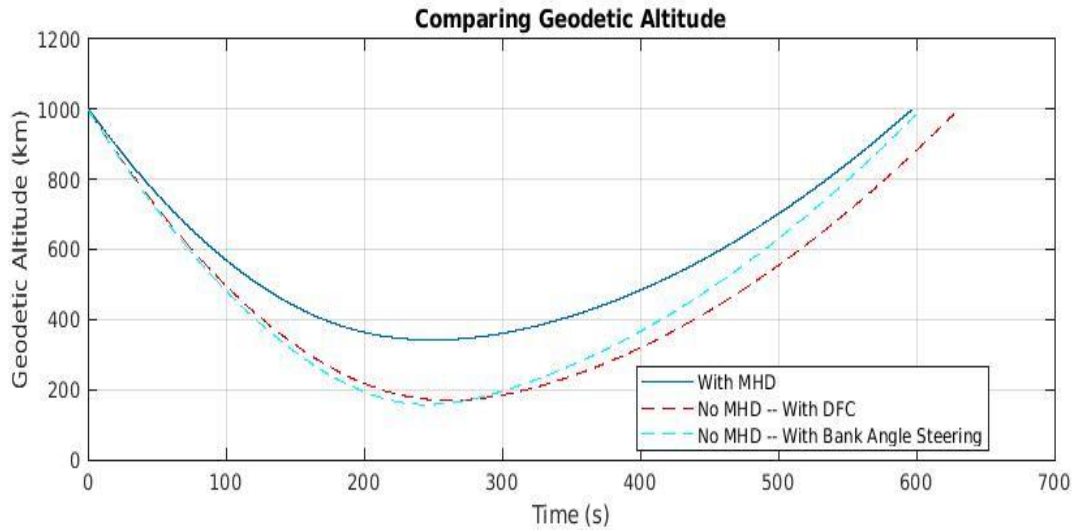

Fig. 8 Geodetic altitude in each control method

Being able to pass at a significantly higher altitude while still retaining the same control authority is a notable feat because it allows the spacecraft to considerably decrease the heat it experiences as it traverses through the atmosphere. The heat flux and total heat load each control method experiences are displayed in Fig. (9) below. As shown, the heat flux for MHD-controlled aerocapture peaks considerably lower than the heat fluxes for the direct force control and bank angle modulation cases. After integrating each plot, the total heat loads are listed as roughly 4,500,000, 4,350,000, and 870,000 kilowatts for the direct force control, bank angle modulation, and magnetohydrodynamically controlled cases, respectively. Thus, the MHD-controlled case successfully reduces the heat load by roughly 80% from the DFC case and approximately 82.4% from the bank angle modulated case. The heat load is directly proportional to the TPS mass; therefore, these results prove that magnetohydrodynamics have the unique advantage over its atmospheric counterparts because of its ability to not only retain control authority and successfully capture but also significantly reduce the TPS mass as well.

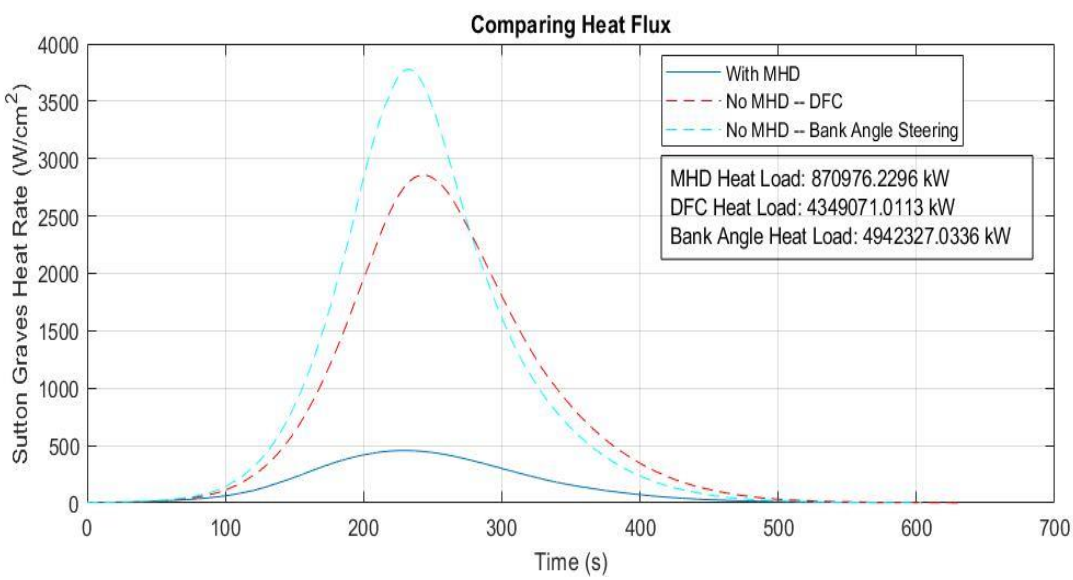

Fig. 9 Heat flux and heat loads for each control method

VII. Conclusion

Throughout this research, magnetohydrodynamically controlled aerocapture has proven to not only have control authority on par with that of DFC or BAM, but it has also shown a unique advantage in its considerably lower heat load and subsequently required TPS mass. While the MHD-induced drag force does not achieve the same order of magnitude as its atmospheric counterparts, it still successfully guides the spacecraft towards the target orbit within a similar amount of time, and it even decreases the sensed acceleration while doing so. These results prove MHD-control as a viable option and even a potentially better alternative over the tradition atmospherically controlled methods.

While magnetohydrodynamics shows promise to serve as the primary option for future larger and farther missions, it is important to note that these results are only for a nominal case tuned to a specific electromagnet configuration, and other configurations may require steeper flight path angles and thus have higher heat loads. However, for this specific point design, these savings are found to be true. Future research may refine this work in three main ways: the electromagnet design, the electrical conductivity model, and the guidance algorithm.

First, the electromagnet design may be further optimized to find the best combination of parameters which minimizes the mass and power while maximizes the magnetic field strength and fusing time. Furthermore, researchers can consider electromagnetic configurations where the electromagnets are not placed at the center of gravity. While this served as a reasonable simplification for this proof of concept, in reality, the electromagnetic configuration should ideally be placed closer to the ionized plasma to maximize control authority. Next, the electrical conductivity model had to be extrapolated below the range of 10^{-6} kg/m^3 because of the complex direct simulation Monte Carlo solvers required for the rarefied flow below that density. While this extrapolation served as a good initial estimate for this research, a more precise model would refine these results even further. Next, although an open-loop guidance algorithm suffices for a proof of concept, active closed-loop guidance is ideal in actual aerocapture applications. Thus, future research should aim to apply some numerical predictor-corrector algorithm to actively change the MHD pitch angle or even the magnetic field vector magnitude to optimize the targeting solution. Finally, while this nominal case succeeds in displaying the capabilities and potential advantages of magnetohydrodynamics, the spacecraft's initial conditions and the planet's atmosphere are dependent on numerous factors and subject to a bit of randomness the nominal model cannot encompass. Therefore, off-nominal Monte Carlo case studies perturbing the spacecraft's initial conditions and aerodynamic model as well as the planet's atmospheric model would prove these results and advantages are true in all conditions.

References

[1] Deshmukh, R., "System Analysis of a Numerical Predictor-Corrector Aerocapture Guidance Architecture," Doctoral Dissertation, Georgia Institute of Technology, August 2019

[2] Lockwood, M. K., "Neptune Aerocapture Systems Analysis," AIAA Atmospheric Flight Mechanics Conference and Exhibit, 2004.
doi: 10.2514/6.2004-4951

[3] Macheret, S., Shneider, M., Candler, G., Moses, R., and Kline, J., "Magnetohydrodynamic power generation for planetary entry vehicles," *35th AIAA Plasmadynamics and Lasers Conference*, 2004.
doi: 10.2514/6.2004-2560

[4] Ali, H., "Magnetohydrodynamic Energy Generation and Flow Control for Planetary Entry Vehicles," Doctoral Dissertation, Georgia Institute of Technology, August 2019

[5] Girija, A. P., "Feasibility and performance analysis of Neptune Aerocapture using heritage blunt body aeroshells (pre-print)," 2020.
doi: 10.31224/osf.io/bxvgz

[6] "Program to Optimize Simulated Trajectories II (POST2)", NASA, https://post2.larc.nasa.gov/

[7] Kelly, C. L., and Little, J. M., "Performance and design scaling of magnetoshells for outer planet drag-modulated plasma aerocapture," *2021 IEEE Aerospace Conference (50100)*, 2021.
10.1109/aero50100.2021.9438387